Numerical analysis of the combustion process of oxymethylene ethers as low-carbon fuels for compression ignition engines

J. M. García-Oliver, R. Novella, C. Micó and D. De Leon-Ceriani

CMT - Motores Térmicos, Universitat Politècnica de València, Camino de Vera s/n, 46022 Valencia, Spain.

Corresponding autor (*): Carlos Micó

e-mail: carmirec@mot.upv.es

Phone: +34 654919619

Abstract

Mitigation of the carbon footprint of internal combustion engines is mandatory to ensure a future for this technology. Within this scope, e-fuels are considered a potential solution to replace conventional fossil fuels. However, in some cases, their physical and chemical properties are so different that its application in conventional engines is complex. For this reason, this work focuses on the study of oxymethylene ethers (OME_X) as a potential low-carbon fuel alternative. The aim is to improve the understanding of the combustion process of these e-fuels when they replace fossil Diesel in internal combustion engines under equivalent operating conditions. To achieve this objective, a computational fluid dynamics model of an optical compression ignition engine has been developed. The operating conditions chosen are representative of a medium load point of the engine, which coincide with experimental work previously done on this platform. n-Heptane was used as surrogate of fossil Diesel while OME_X was simulated as a

simpler mixture of oxymethylene ether molecules. Results show remarkable differences between Diesel and OME_X. This fuel provides lower equivalence ratio fields. Thus, oxidation reactions are promoted in wider areas within the combustion chamber, leading to a faster combustion process. Besides, the soot formation is also drastically decreased in comparison to the other fuel. These results have been corroborated with experimental information.

Keywords

Computer Fluid Dynamics; Oxymethylene Ether; soot reduction; compression ignition; low-carbon fuel.

Abbreviations

aTDC: after top dead centre

CI: Compression Ignition

CO_2: Carbon dioxide

EVC: Exhaust valve closing

EVO: Exhaust valve opening

HVO: Hydrotreated Vegetable Oil

ICE: Internal Combustion Engine

IMEP: Indicated Mean Effective Pressure

IVC: Intake valve closing

IVO: Intake valve opening

LHV: Lower Heating Value

NO_X: Nitrogen oxides

OH: hydroxyl radical

OME_X: Oxymethylene Ethers

SOI: Start of injection

TDC: Top dead centre

1. Introduction

Climate change is one of the most important and difficult challenges that society is facing. This phenomenon is linked to the global warming, which is enhanced by the accumulation in the atmosphere of green-house gases that are mainly produced by the human activity. The greenhouse gas emission trends of the last three decades show a continuous increase of direct and indirect green-house gas emissions reaching a 14% share of the total emissions in 2018, from which road transport represents 73% of it[1]. Besides, recent studies identify this sector as a burden for the climate mitigation efforts[2]. For this reason, researchers and the automotive industry are dedicating big efforts on reducing this carbon footprint.

In this scenario, the search of low-carbon alternatives to conventional fossil fuels has emerged as a very interesting proposal. They drastically reduce the carbon footprint of hydrocarbon powered vehicles, without needing major modifications in terms of the internal combustion engine (ICE) design[3–7]. An alternative that has being developed during the last decade is the so-called e-fuels. This term refers to synthetic fuels that are produced from the combination of

electricity, water and carbon dioxide (CO_2). Their carbon neutrality derives from the fact that, on one hand, the required electricity is obtained from renewable energy sources. On the other hand, the amount of CO_2 released during its use is only as much as the one used for its production[6,8]. Some authors have already highlighted the relevant role that the e-fuels would have for the transportation sector but also as a way to store and transport renewable energy[6,9,10]. Even certain scenarios consider them necessary to achieve the CO_2 reduction targets in combination with other solutions[9]. Interest has been recently gained by oxymethylene ethers (OME_X). Different life-cycle assessments reported the potential reduction of greenhouse gas emissions of these fuels in comparison to conventional Diesel[11–13] either completely or partially replacing fossil fuels. However, the use of renewable energies is the key to achieve this.

The OME_X are hydrocarbons formed by a chemical structure CH_3-O-$(CH_2$-O$)_X$-CH_3, where X usually varies from 1 to 6. Thanks to the oxygen content and the absence of C-C bonds, these fuels have potential to reduce soot emissions in engines. OME_1 is the simplest molecule of the OME family. However, according to Härtl et al.[14], this fuel cannot be used unblended. In contrast, longer chain OME_X are more interesting as they have more suitable properties[15]. Different works have reported an important reduction of in-cylinder soot formation emissions either using neat OME_X or blending it with other fuels[16–19]. Additionally, several authors reported the possibility of using of EGR to reduce nitrogen oxides (NO_X) emissions without affecting soot emissions[14,20], overcoming the well-known Soot-NO_X trade off. As a drawback, OME_X has a lower heating value (LHV) lower than fossil Diesel. Thus, higher injection pressures and/or durations are necessary to compensate the energy decrease. However, combustion duration is shorter thanks to a faster burnout, which can improve thermal efficiency[15,21,22]. In this regard, however, it has been also observed that the longer injection durations could lead to longer combustions under certain operating conditions, which will cause a reduction of the efficiency[23]. In addition, an increase of certain emissions like carbon monoxide or hydrocarbons has been also reported when using this fuel[24].

Considering all the interest, the objective of the current work is to provide more insight into the potential of OME_X fuels to power ICE engines replacing fossil Diesel. For this purpose, a numerical study has been performed with the commercial code CONVERGE, with a domain based on a single cylinder optical compression ignition engine geometry. The novelty of this research resides on the lack of numerical studies of multicomponent OME_X not blended with other fuels, under realistic engine operating conditions. The main contribution of this work is to provide a detailed description of the impact of the oxygen content and stoichiometry of the oxymethylene ether molecule on combustion development, energy release and soot formation/oxidation in comparison with more conventional fuels. The results provide details with spatial and temporal resolution about the equivalence ratios reached by OME_X in comparison to Diesel and their impact on the evolution of the combustion process, paying special attention on aspects like the energy release or the late combustion stage. The comparison between both fuels is performed under equivalent engine operating conditions, which implies a different injection strategy that could affect OME_X performance. Besides, results are supported by experimental data obtained in the same optical engine used as model for this research (Pastor et al.[25]), which has not been observed in previous publications related with neat OME_X.

2. Modeling approach

2.1. Fuel definition

The aim of the current work is to analyse the behaviour of OME_X when replacing fossil Diesel in a CI engine. For this purpose, simulations of the alternative and the fossil fuel have been carried out under the same operating conditions. For fossil Diesel, the liquid phase was simulated using a pre-defined fluid from the commercial code CONVERGE[26] (identified as DIESEL2). For the vapor phase, n-Heptane was chosen as it is a widely accepted surrogate for this fuel[27–29] as it provides similar ignition delay values to those of n-alkanes with carbon atoms in the range of 7 to 16[30,31].

112 The definition of the OME_X surrogate fuel was done to represent the fuel corresponding to the
113 experimental data that has been used in this study, which was a mixture of different chain
114 lengths where the larger fractions corresponded to OME_3 and OME_4. The OME_5 and OME_6
115 molecules were excluded as it was not possible to obtain from literature the physical properties
116 required to simulate them. Besides, the reaction mechanism used only included from OME_2 to
117 OME_4. Thus, it was decided to define the surrogate fuel as a blend of OME_3 and OME_4, using the
118 second one as representative of all OME_X fractions with $X \geq 4$. The composition of the reference
119 fuel and its surrogate (OME_{3-4}) are included in Table 1. The main properties of the original fuels
120 and their surrogates are summarized in Table *2*.

121 Table 1 Composition of OME_X and OME_{3-4}

Molecule	OME_X (wt%)	OME_{3-4} (wt%)
OME_1	0.01	0
OME_2	<0.01	0
OME_3	57.90	57.9
OME_4	28.87	42.1
OME_5	10.08	0
OME_6	1.91	0

122 Table 2 Original and surrogate fuel main properties

Properties	Diesel	n-Heptane	OME_X	OME_{3-4}	DIESEL 2
Density [kg/m^3] (T= 15 °C)	835.20	688.43	1057.10	1044.74	848
Viscosity [mm^2/s] (T= 40 °C)	2.80	0.52	1.08	2.09	2.59
Cetane number [–]	54.18	56 [32]	68.6	-	-
Lower heating value [MJ/kg]	39.79	44.91	19.21	19.89	-
Initial Boiling Point [°C]	155.10	98.42	144.90	155.04	268.78
Final Boiling Point [°C]	363.1	-	242.4	201.1	-

Carbon content [% m/m]	85.3	84	44.2	43.8	-
Hydrogen Content [% m/m]	13.4	16	8.8	8.7	-
Oxygen content [% m/m]	0	0	45	47.5	-
Air/Fuel stoichiometric ratio	14.39:1	15.18:1	5.89:1	5.98:1	

For each fuel, a different injection rate was used that was defined based on the injection strategies used in the reference experimental study[25] and are represented in Figure 1. For the two fuels, the injection strategy was made up by 2 pilot injections, the main injection and a post-injection. The start and duration of each injection event, as well as the injection pressure, were experimentally set to obtain 7.5 bar IMEP and a similar combustion phasing for both fuels. Due to the different LHV, OME_X required a longer main and post injection. Finally, it is worth mentioning that the injection rate was scaled for the two surrogate fuels, based on the ratio between their LHV and the original fuel's one. More specifically, for n-Heptane it means a 12% reduction of injected mass in comparison to Diesel while for $OME_{3\text{-}4}$ it means a 3.5% of reduction compared to OME_X.

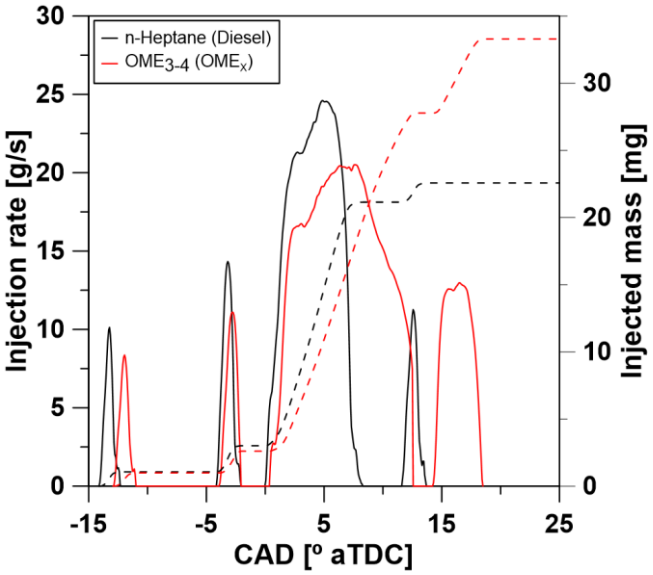

Figure 1 Mass flow rate (continuous line) and injected mass (dashed line) for the two surrogate fuels

2.2. Computational set-up

A 3D model of an optical single cylinder compression ignition engine has been used to define the computational domain. It is based on a commercial engine platform[25] with 400 cm^3 unitary displacement. The model also replicates the original cylinder head installed in the optical engine, with 4 valves per cylinder and a centrally located injector. The bore and stroke are also the same as the original engine. The main geometry parameters are summarized in Table 3.

Table 3 Optical engine main parameters

Valves per cylinder [-]	4
Num. of cylinders [-]	1
Stroke [mm]	80.1
Bore [mm]	80
Unitary displacement [cm^3]	402
Effective Compression ratio [-]	10.4
Bowl type [-]	Re-entrant
Intake valve distribution [° aTDC]	IVO:380.21; IVC: -157.31
Exhaust valve distribution [° aTDC]	EVO:175.52; EVC: 367.8

The computational domain includes the combustion chamber and the intake and exhaust ducts. It is represented in Figure 2. Besides, intake and exhaust lines of the experimental facility have been also included to properly define intake and exhaust boundaries and to simulate a realistic air-flow management process.

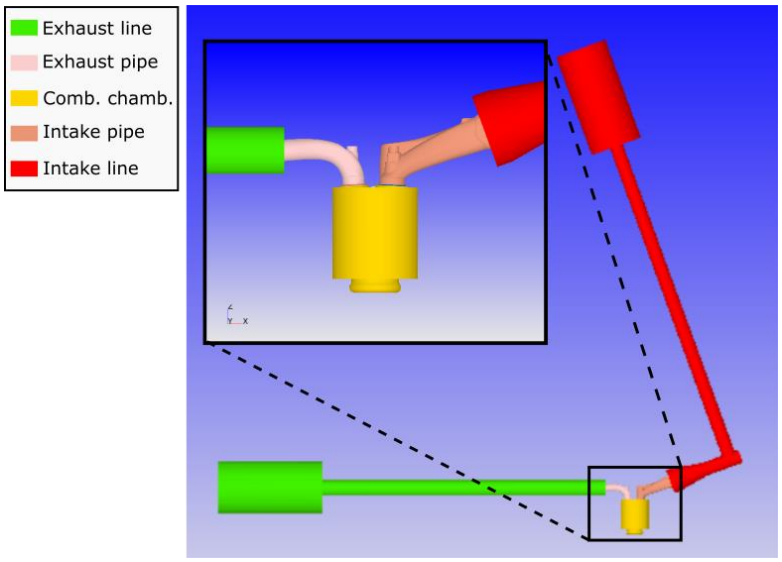

Figure 2 Sketch of the computational domain

To define the computational domain meshing, a mesh sensitivity analysis was performed. Its effect over in-cylinder pressure and heat release rate (HRR) were used as reference. Different base grid sizes were evaluated, using the same mesh configuration. For all of them, a grid refinement was applied to all in-cylinder surfaces to properly model the boundary layer and heat-transfer. A similar configuration was applied to the valve seat and valve head surfaces due to the strong velocity gradients that could be expected in this region. Besides, additional grid refinement was applied to the volume occupied by fuel sprays to improve break-up, evaporation and combustion modelling accuracy. This was used from start of injection (SOI) until 20° aTDC. Finally, an adaptive mesh refinement algorithm was also used at the in-cylinder region and the intake and exhaust ports. It automatically applied a mesh refinement to keep gradients of certain parameters below pre-defined maximum values. In this case, velocity and temperature were configured as the reference parameters. The Table 4 shows a summary of the different meshes evaluated.

Table 4 Summary of the different meshes evaluated in the mesh sensitivity analysis

Molecule	Mesh A	Mesh B	Mesh C	Mesh D

Base grid size (mm)	1	0.8	0.6	0.4
Number of cells at top dead centre	164,941	272,513	586,891	1,657,044
Computational time (h)	3.4	8.2	29.7	79.7

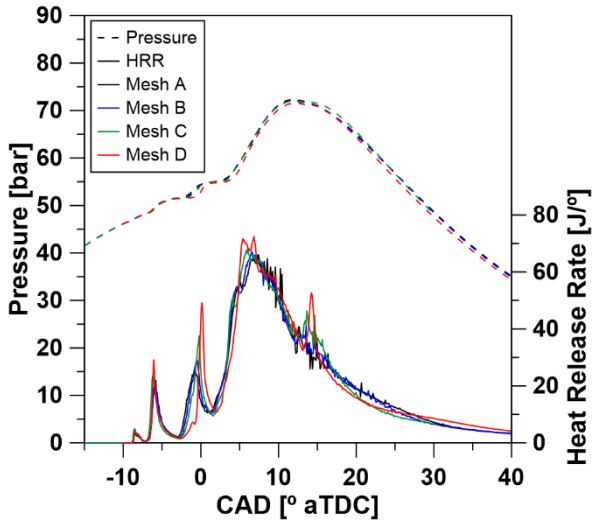

Figure 3 In-cylinder pressure and heat release rate of n-Heptane corresponding to the mesh sensitivity analysis

The results obtained with all the meshes are summarized in Figure 3. In terms of in-cylinder pressure, there are no remarkable difference among them. However, it is possible to see that Mesh A and B are not able to reproduce the last HRR peak that corresponds to the post-injection combustion. In contrast, the other two meshes can reproduce this event. Small differences can still be detected between Mesh C and D, as slightly higher HRR peaks are obtained for the second one during the second pilot and the post-injection combustion. When looking at the computational cost, for n-Heptane the Mesh D requires 2.7 times more time. However, for $OME_{3\text{-}4}$ the computational time required with this mesh was estimated to be around 640 hours due to the complexity of its mechanism. For this reason, the 0.6 mm base grid size has been chosen as it was able to provide similar results to those of a finer mesh and reproduce the characteristic events of the combustion process, while keeping an affordable computational cost.

In terms of multiphase modelling, the available Lagrangian parcel - Eulerian fluid approach in CONVERGE[26] has been used. The description of the Eulerian fluid is made using the Reynolds-Averaged Navier-Stokes (RANS) Re-Normalization Group (RNG) k-epsilon model. The heat transfer through walls was modelled with the O'Rourke & Amsden model[33]. The Pressure implicit with splitting of operators (PISO) density-based solver scheme was used. As for the Lagrangian liquid phase, evaporation was simulated by using the Frossling correlation with a uniform temperature model for droplets[34] and the uniform temperature film vaporization model[35]. For the spray breakup, the Kelvin-Helmholtz breakup model[36] with child parcel creation and the Rayleigh-Taylor breakup model[37] with breakup length were used. The injected drop diameter was defined as the same of the nozzle orifice (blob). The drop/wall interaction was resolved by means of the Rebound/slide wall impingement model[38]. The No Time Counter (NTC) method[39] was used to take into account the effect of droplet collisions. To properly define the drop drag phenomenon, a dynamic model was used that accounted for variations in the drop shape through a distortion parameter[35]. The configuration chosen was based on the one tested by Desantes et al.[40], which has been used in later studies with OME_{3-4}[41].

Two different types of simulations were carried out. The first one (motored simulation) was configured to start at top dead centre (TDC), at the beginning of the intake stroke, and extended through the motored cycle until the intake valve closing event (IVC). The main purpose was to simulate the air management process and calculate the in-cylinder velocity field that was used to initialize the air movement for the combustion simulation. This is the second simulation type, which included spray, combustion and soot formation modelling. However, in some cases as mentioned below in the discussion section, combustion was deactivated. This one started at IVC and lasted until the exhaust valve opening event (EVO).

Boundary conditions were defined based on experimental data. An in-house developed zero-dimensional single-zone thermodynamic model[42] was used. Starting from experimental data

such as in-cylinder pressure or intake air mass-flow rate, the model can calculate thermodynamic conditions at IVC which are used to initialize pressure and temperature fields for the combustion simulation. Besides, it can estimate different parameters related with heat transfer, like in-cylinder surface temperatures. It applies a nodal model to calculate mean temperature of the liner, the piston and the cylinder head which were used as the boundary conditions to model the heat transfer problem.

An injector with an 8-hole nozzle was used for the simulation. The orifice diameter was 116 µm, with a constant discharge coefficient of 0.85. The angle between the spray axis and the cylinder head plane was set to 22.5°. It was estimated based on the characterization of the same engine presented by Pastor et al.[43]. The injection timing and the footprint created by the sprays on the piston was used to calculate it. Besides, the spray cone angle was set to 15.25°, as obtained from high-speed images registered in the optical engine.

Combustion has been simulated using the well-mixed SAGE detailed chemical kinetics solver[44]. Thus, for each of the fuels used in this work a specific reaction mechanism was utilized. For OME_{3-4}, the mechanism published by Cai et al.[45] was chosen as it was developed to simulate from OME_2 to OME_4. However, this mechanism does not contain n-Heptane. Thus, an additional one was selected for this purpose (Nordin[46]). Soot formation and oxidation was simulated with the Hiroyasu empirical soot model[47], with C_2H_2 as soot precursor.

2.1 In-cylinder operating conditions

A single operating point has been simulated for both fuels. It is representative of a medium load point (7.5 bar IMEP) of the optical engine. Experimental intake pressure and temperature were set to 2.15 bar and 94°C to compensate for the low compression ratio of the engine. This resulted in 2.21 bar and 100.49°C at IVC, which were used to initialize pressure and temperature fields in the computational domain. In Figure 4, the simulated in-cylinder pressure evolution is

compared with the experimental one between -20 and 40° aTDC for both motored and combustion conditions. It is possible to see that the in-cylinder thermodynamic conditions are accurately simulated during the whole injection event. Only a small discrepancy starts appearing during expansion stroke. In addition, the comparison between the experimental and simulated reactive pressure curves show that the mechanisms and the model configuration chosen are able to reproduce the relative experimental behaviour of both fuels while the difference with the experimental data is around 5% close to the peak pressure.

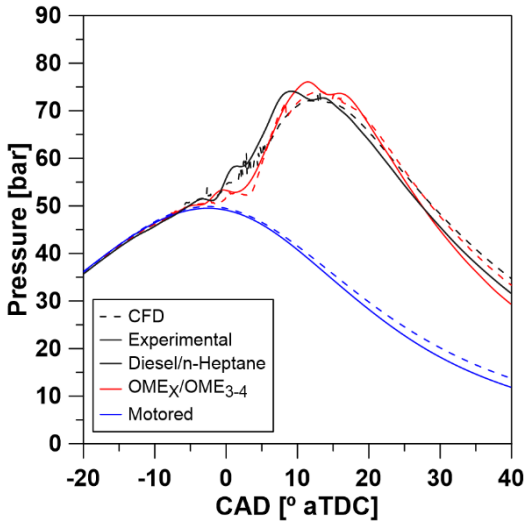

Figure 4 Comparison between experimental and calculated in-cylinder pressure evolution for both fuels under motored and combustion conditions.

3. Results and discussion

3.1. Mixture formation.

With the aim of following the chronological order of events that take place after SOI, discussion will start with the analysis of air/fuel mixture formation for cases where the combustion model was not activated. The evolution of the evaporated fuel mass fraction distribution is shown in Figure 5. It must be noted that the analysis is focused on the main and post-injection events. Information corresponds to a plane perpendicular to the piston movement and oriented so it is aligned with the symmetry plane of two opposed sprays.

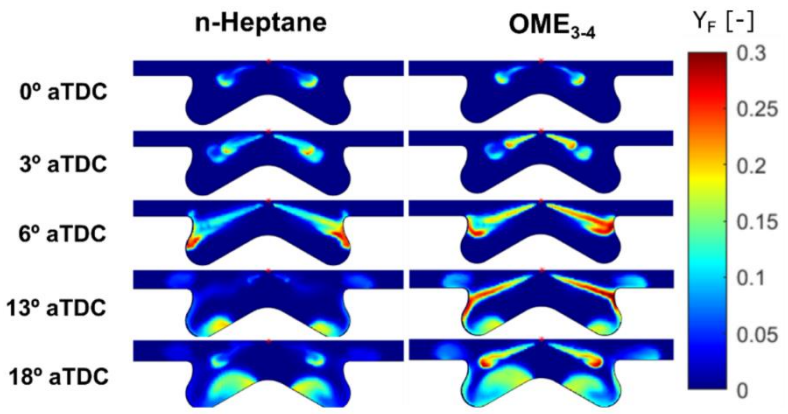

243

244 Figure 5 Evaporated fuel mass fraction evolution for n-Heptane and OME_{3-4} at different instants.

245 Until 6° aTDC, injection strategy is quite similar as it is shown in Figure 1. Thus, although OME_{3-4}
246 injected mass is slightly lower, a similar distribution is observed. After this timing, the end of the
247 main injection is reached for n-Heptane while for OME_{3-4} fuel delivery is still on-going. This
248 results in the decrease of the mass fraction fields for the first one, with high concentrations
249 remaining close to the bowl periphery. As for OME_{3-4}, higher mass fraction values are still
250 observable for a longer time due to the longer injection event.

251 Despite OME_{3-4} has different physical properties, they seem to not affect evaporation and
252 mixture formation in comparison to Diesel. However, its molecule contains a large amount of
253 oxygen atoms which defines a very different stoichiometry compared to n-Heptane. Thus, even
254 if the OME_{3-4} evaporated mass fraction distribution were similar, it could be expected that the
255 equivalence ratio (ϕ) will not be so. For this reason, the ϕ distribution of n-Heptane and OME_{3-4}
256 are compared in Figure 6. Values have been calculated only with evaporated fuel, to be
257 consistent with Figure 5. Besides, data corresponds to the same plane used in that figure. Due
258 to the different stoichiometry, ϕ levels of OME_{3-4} are much lower than those of n-Heptane. Even
259 after the end of the main injection of this fuel, the oxymethylene mixture still provides lower ϕ
260 values being bellow 2 even at the spray symmetry plane. At this point, it is worth mentioning
261 that the injection rate escalation based on LHV is reducing the differences between fuels in

comparison with those that could have been obtained in experiments. However, still much lean mixtures are achieved by OME_{3-4} which hint at a potential soot-free combustion process.

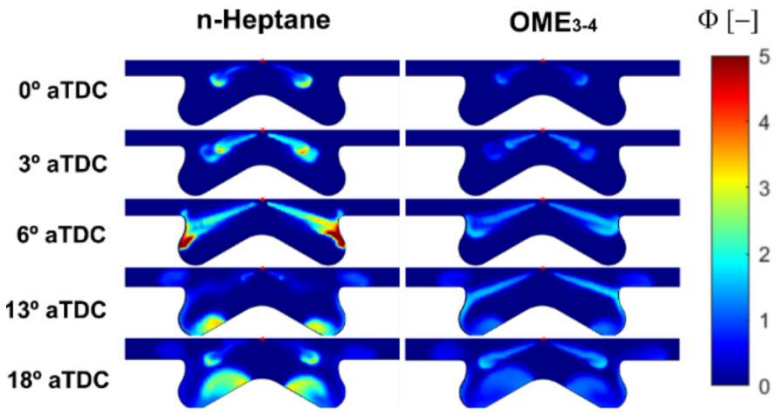

Figure 6 Equivalence ratio (ϕ) evolution for the for n-Heptane and OME_{3-4} at different instants.

3.2. Combustion and soot formation

The simulation of the combustion process allows to obtain the HRR for each fuel, which is shown in Figure 7. The plot on the left corresponds to the data obtained from the CFD calculations while the plot on the right represents the experimental data reproduced from Pastor et al.[25].

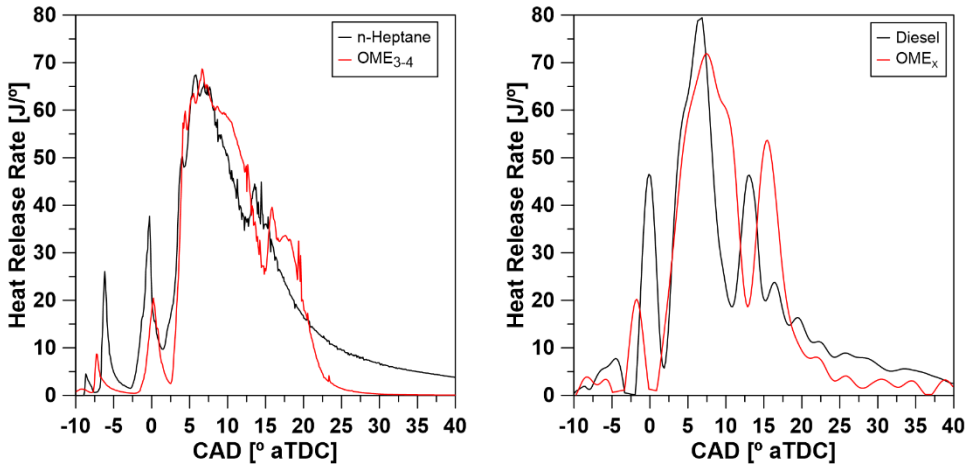

Figure 7 Experimental (right) and calculated (left) heat release rate for Diesel and OME_X and their surrogates. Information reproduced from Pastor et al[25].

Once the two pilot injections have burned, in-cylinder conditions promote the combustion of the main injection event for both fuels. Focusing on this part of the combustion process, it is possible to see that n-Heptane and OME_{3-4} present a relative behaviour like what it is observed when comparing experimental Diesel and OME_X data. During main injection combustion, between 2.5 and 12.5° aTDC, the same HRR peak value is achieved by n-Heptane and OME_{3-4} at the simulation while a small difference is observed in the experimental data. The effects of the different injection strategy are also visible, with a longer main injection event and a later post-injection for the OME_{3-4}. However, it is possible to see that the late stage of combustion is much faster for this fuel in comparison to n-Heptane. The slope of the HRR curve is more pronounced after the post-injection and it drops to zero much earlier. This behaviour is observed both in the simulation and experiments. Similar differences were reported by Pastor et al.[48] when comparing pure Diesel with different mixtures of this fuel and OME_X as well as neat OME_X.

In Figure 8, the spatial distribution of the accumulated hydroxyl radical (OH) mass between the piston and the cylinder head surface is shown for both fuels. This data should be comparable with the OH* chemiluminescence radiation, which is known to be a good tracer of high-temperature oxidation reactions[49]. Radiation was registered through the optical access of the piston bowl and it is represented in Figure 9. These images are the result of the accumulation of all radiation emitted by this excited radical all along the combustion chamber. The intensity scale used for each instant was adjusted to avoid saturation.

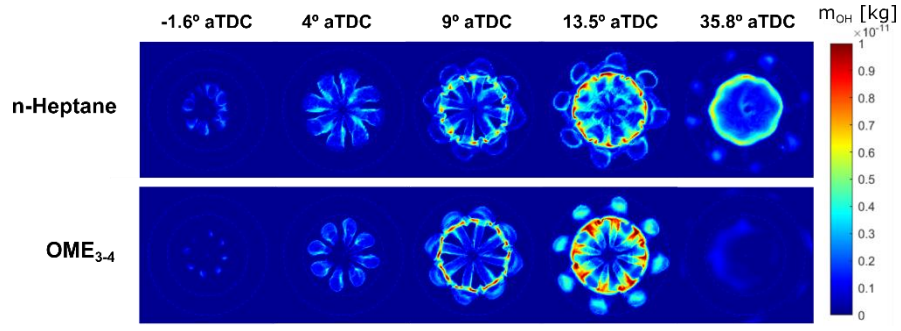

Figure 8 Accumulated OH mass distribution for n-Heptane and OME_{3-4} at different instants.

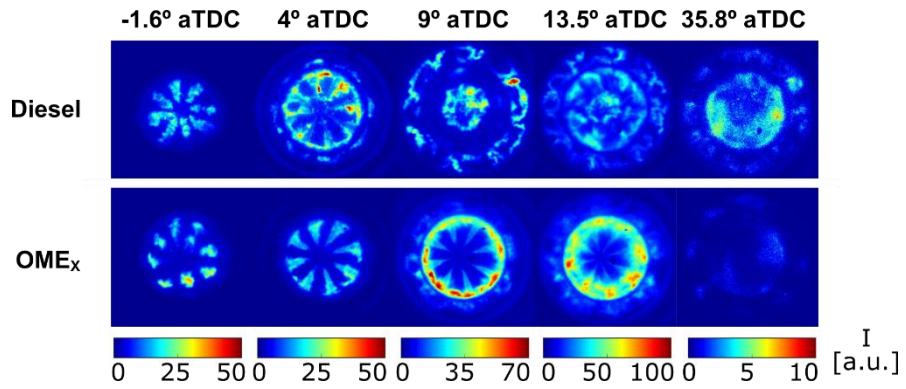

Figure 9 OH* radiation measured for Diesel and OME_X at different instants. Information reproduced from Pastor et al[25].

When comparing experimental results and simulations, several similarities can be identified. Between the start of combustion and 5° aTDC, OH is located mainly in the bowl for both fuels as it is shown by both experiments and CFD. At -1.6° both data sources provide slightly different distributions, showing the experiments larger areas than the simulations. This is coherent with the discrepancies observed with the HRR for the pilot injection combustions. Nevertheless, for both CFD and experiments it is possible to see that Diesel and n-Heptane show higher OH presence than OME_X and OME_{3-4}, which is coherent with the HRR evolution observed in Figure 7. Just after 4° aTDC, the main injection combustion has started and HRR is rising. The combustion extends and grows faster for OME_{3-4} and the OH quantity increases over n-Heptane. At 9° aTDC, remarkable differences appear in the experiments as Diesel shows almost no OH* signal in the bowl even at its periphery. This is not consistent with simulations. Nevertheless, the authors of the experimental work stated that the presence of high amounts of soot close to the bowl bottom could be screening the ultraviolet radiation at this stage of combustion, which explain the differences with the results presented here. At 13.5° aTDC, n-Heptane still presents a different OH distribution in comparison to OME_{3-4}. The first fuel shows high OH presence close to the bowl wall and the squish region. However, for the second fuel not so much OH is observed at the squish region while inside the bowl the high OH regions extend towards the piston centre as combustion evolves. This behaviour is observed in both simulation and experiments.

315 The previous description of the OH distribution for each fuel suggest that, after 13.5° aTDC, OH
316 is present in larger regions for OME_{3-4} in comparison to n-Heptane. The oxygen content in the
317 first fuel allows the air-fuel mixture to be closer to the stoichiometric ratio ($\phi = 1$) and even
318 bellow it in larger areas of the combustion chamber, as it was observed in Figure 6. This increases
319 locations where fuel is likely to be oxidized, which would lead to a higher global oxidation rate
320 of OME_{3-4} during the main injection combustion stage. At this point, it is worth mentioning that
321 too low ϕ values could lead to a slowdown of the combustion process. However, the fact that
322 this fuel reaches similar HRR levels to those of n-Heptane despite its lower LHV confirms that
323 this is not the case. In contrary, it suggests even a faster reaction progression. The high reactivity
324 of OME_{3-4} is playing a major role in this scenario as it allows the combustion to progress even
325 under unfavourable conditions such as excessive low ϕ values. Additionally, the faster final
326 oxidation that was reported with the HRR can be considered also evidence of this behaviour.
327 This is also observed when comparing OH distribution at 35.8° aTDC for both simulations and
328 experiments, as almost any OH trace is observable for OME_X while it is still detectable for Diesel.
329 Besides, a similar behaviour has been previously reported[15,21].

330 In Figure 10 the OH mass fraction distribution is shown for the two fuels, at the same plane
331 represented in previous figures. Besides, a contour line has been included which corresponds to
332 $\phi = 1$, to highlight the mixing distribution. Between 5 and 10° aTDC, OH is located at the
333 periphery of the flame for all the cases, which corresponds to the location of stoichiometric
334 region. This is a characteristic structure of diffusion flames as described by Dec et al.[49]. From 20°
335 aTDC onwards, fuel has reached the bottom of the bowl and the squish region as it is shown in
336 Figure 5. In this situation, it is possible to see for n-Heptane that OH is still located at the edges
337 of the fuel regions, either from the remaining spray structure or from the fuel clouds inside and
338 outside the bowl. In all these regions, there is a correspondence between the $\phi = 1$ contour line
339 represented and the OH location. However, for OME_{3-4} the situation is different. In this case, it
340 is possible to see larger regions with high OH presence that coincide with relatively high fuel

concentration locations. Based on the contour lines reproduced, it is possible to see that most of these regions present $\phi < 1$ and only rich mixture can be found within the post-injection spray and in a small region close to the bowl floor, where no OH is observed. When moving to 25° or 35° aTDC, OME_{3-4} shows a lean mixture in all the combustion chamber, while n-Heptane still presents large rich mixture areas. These results confirm the impact of the different stoichiometry of the OME_{3-4} on combustion development which, in combination with its higher reactivity, generates large regions where the fuel is oxidized with consequences in terms of HRR and combustion duration that have been already highlighted.

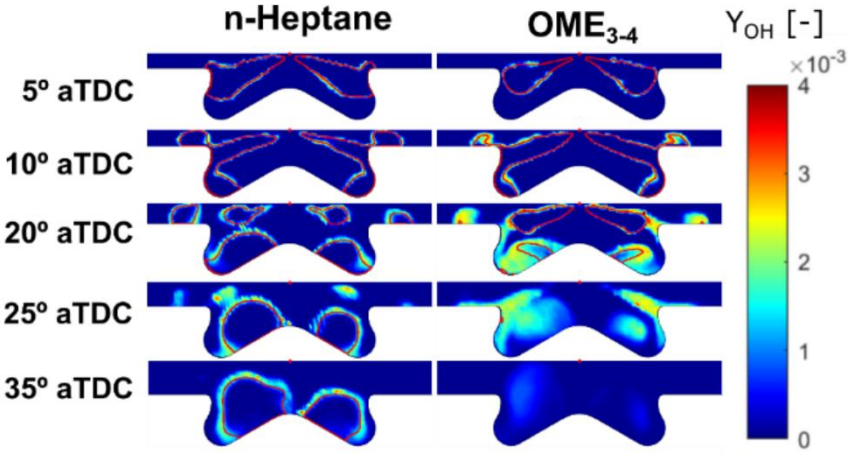

Figure 10 OH mass fraction evolution for n-Heptane and OME_{3-4} at different instants. The red line represents the ϕ = 1 contour.

To highlight and summarize the differences in stoichiometry between OME_{3-4} and n-Heptane, ϕ-T maps have been represented in Figure 11 for the two fuels at 10, 20 and 35° aTDC. Data corresponds to combustion simulations and represent the whole combustion chamber. OME_{3-4} shows, in general, lower equivalence ratio values than n-Heptane. In fact, it does not reach the soot peninsula, which agrees with previous experimental works where no soot formation was measured for OME_X[25,50]. On the other hand, n-Heptane reaches $\phi > 2$ at certain regions, which can lead to soot formation. When looking at the temperature, it is possible to see that for 10 and 20° aTDC both fuels reach similar levels, entering the NO_X region. However, at 35° aTDC the

360 temperatures for OME_{3-4} have significantly decreased in comparison to n-Heptane thanks to the
361 faster oxidation process that has been previously discussed.

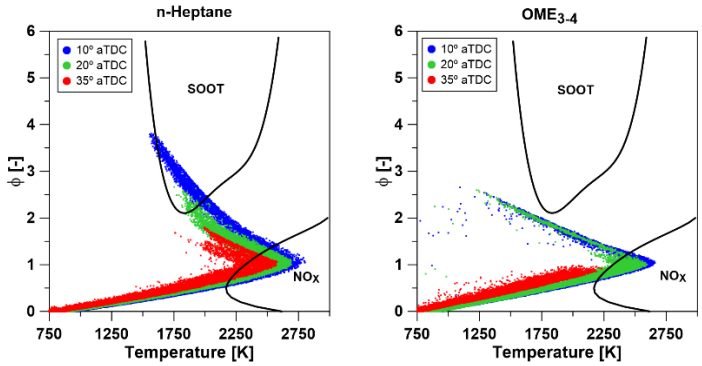

362

363 Figure 11 Equivalence ratio vs. Temperature maps for n-Heptane and OME_{3-4} at 10, 20 and 35º aTDC.

364 Finally, soot model results are presented here to compare the different fuel behaviour but some
365 considerations need to be made, though. On the one hand, the molecule structure of the
366 surrogate fuels should have strong impact on soot formed. In this work, n-Heptane was chosen
367 as Diesel surrogate as it is known to be able to reproduce a similar combustion behaviour.
368 However, Diesel contains aromatic compounds that are known to be soot precursors.
369 Additionally, the longer hydrocarbon chains of this fuel would produce more soot than the
370 surrogate one. On the other hand, different authors have reported that Hiroyasu model could
371 be not accurate enough to quantify soot formation[51]. Besides, the reaction mechanism chosen
372 can also determinate results in this regard[52]. However, the approach chosen is considered good
373 enough to compare such different fuels as n-Heptane and OME_{3-4} in a qualitative way.

374 Soot formation and oxidation behaviour for the two fuels have been analysed in terms of soot
375 (red) and OH (blue) distribution in Figure 12. Data corresponds to both species mass fraction on
376 a plane perpendicular to the piston movement (the same plane used in previous figures). Values
377 have been normalized between 0 and 1, based on the maximum values reached at every instant
378 for each fuel, to improve its visibility and focus on the spatial distribution in the combustion
379 chamber. However, it is important to highlight that the soot model predicts two orders of

magnitude less soot for OME_{3-4} than for n-Heptane. This agrees with the results reported by Pastor et al. in[25,50], where it was not possible to measure any soot formation for OME_X.

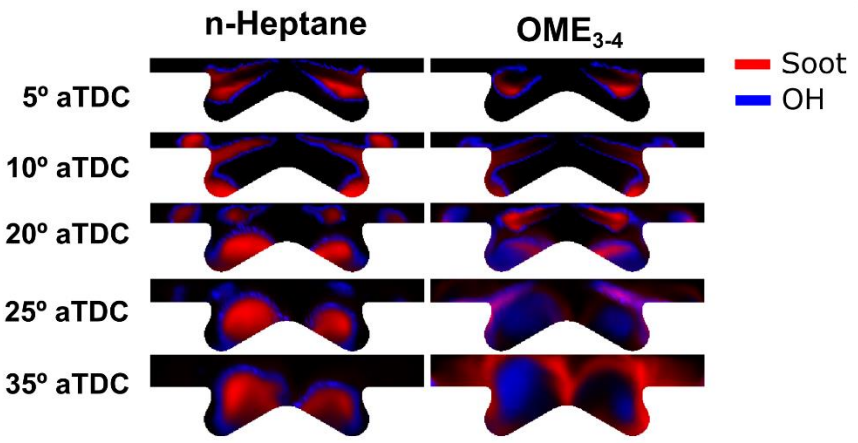

Figure 12 Normalized soot (red) and radical hydroxyl (blue) distribution for n-Heptane and OME_{3-4} at different instants.

Until 10° aTDC, both fuels show a similar OH and soot distribution. The first specie is located mainly at the periphery of the flame while the second one appears within this frontier. From 20° aTDC onwards, there is a remarkable change in OME_{3-4}. While for n-Heptane OH is still located around $\phi = 1$ as shown in Figure 10, with the OME_{3-4} this radical extends to wider regions where $\phi < 1$. This is especially visible at the bottom of the bowl, where OH and soot seem to be overlapped. According to the simulations under inert conditions, these regions are where the fuel tends to accumulate. These results are in agreement with Goeb et al.[53], who state that OME_1 resulted in leaner mixtures as reported here and shifted the reactions and soot precursor formation to higher mixture fractions, which are avoided as mixing and combustion progresses. These authors state that this is the main cause for the remarkable soot formation reduction achieved with oxymethylene ethers even when they are blended. At 35° aTDC, it is possible to see that soot and OH distributions are somehow inverted. While n-Heptane presents large amounts of soot at the bottom of the bowl that are difficult to oxidize, with OME_{3-4} this region

398 is occupied by OH. In this case, soot is relegated to other areas of the combustion chamber, and
399 it will be oxidized before the end of combustion.

400 **4. Conclusions**

401 The aim of this work has been to evaluate the behaviour OME_X as a potential low-carbon fuel
402 alternative to fossil Diesel. For this purpose, CFD simulations of an optical engine have been
403 carried out with two surrogate fuels: n-Heptane (Diesel) and OME_{3-4} (OME_X). Besides,
404 experimental data obtained at the same optical engine has been used to corroborate CFD
405 results.

406 The first simulations under inert conditions highlighted the great relevance of the different
407 stoichiometry of each molecule. While the in-cylinder fuel distribution is similar for the two
408 fuels, the equivalence ratio is not. The oxygen content of the OME_{3-4} allows to keep equivalence
409 ratio bellow 2 almost all along the combustion chamber, which has a strong impact on the
410 combustion process.

411 The existence of higher amount of fuel under ϕ values close to 1 with OME_{3-4} means that there
412 is more fuel likely to be oxidized. The high reactivity of the fuel is playing a major role in this
413 process as it avoids combustion slowdown caused by too low ϕ values. The larger OH regions
414 obtained in the simulations and confirmed with the experimental data reaffirm this idea, as this
415 radical is considered a good tracker of the high temperature oxidation reactions. The first
416 consequence is that in-cylinder overall fuel oxidation rate is higher compared to n-Heptane. In
417 fact, it even compensates its lower LHV making the HRR to reach similar values as the other fuel,
418 which was observed in both simulation and experimental data. The second consequence is that
419 combustion finishes faster, even for a longer injection, which suggest that using different
420 injection strategies could be a solution to compensate the lower energy available in the fuel
421 when using OME_X to replace Diesel.

Finally, it has been observed that OME_{3-4} reacts under low ϕ values that result in extensive oxidation regions and very low soot formation. Simulations suggest that much less soot is formed with this fuel, which is coherent with the impossibility to detect any soot in the experimental work.

5. Bibliography

1. Lamb WF, Wiedmann T, Pongratz J, et al. A review of trends and drivers of greenhouse gas emissions by sector from 1990 to 2018. *Environ Res Lett* 2021; 16: 073005.
2. Lamb WF, Grubb M, Diluiso F, et al. Countries with sustained greenhouse gas emissions reductions: an analysis of trends and progress by sector. *Clim Policy* 2022; 22: 1–17.
3. Xue J, Grift TE, Hansen AC. Effect of biodiesel on engine performances and emissions. *Renew Sustain Energy Rev* 2011; 15: 1098–1116.
4. Arcoumanis C, Bae C, Crookes R, et al. The potential of di-methyl ether (DME) as an alternative fuel for compression-ignition engines: A review. *Fuel* 2008; 87: 1014–1030.
5. Ramadhas AS, Jayaraj S, Muraleedharan C. Use of vegetable oils as I.C. engine fuels - A review. *Renew Energy* 2004; 29: 727–742.
6. Schemme S, Samsun RC, Peters R, et al. Power-to-fuel as a key to sustainable transport systems – An analysis of diesel fuels produced from CO2 and renewable electricity. *Fuel* 2017; 205: 198–221.
7. Ghazikhani M, Hatami M, Safari B, et al. Experimental investigation of exhaust temperature and delivery ratio effect on emissions and performance of a gasoline–ethanol two-stroke engine. *Case Stud Therm Eng* 2014; 2: 82–90.
8. Yasari E, Panahi M, Rafiee A. Multi-objective optimization and techno-economic analysis of CO2 utilization through direct synthesis of di-methyl ether plant. *Int J Energy Res* 2021; 45: 18103–18120.

9. Rothbart M. e-Fuel Production via Renewables and the Impact on the In-Use CO 2 Performance. In: *SAE Technical Papers*., 2020: 2020-01-2139.

10. Varone A, Ferrari M. Power to liquid and power to gas: An option for the German Energiewende. *Renew Sustain Energy Rev* 2015; 45: 207–218.

11. Mahbub N, Oyedun AO, Kumar A, et al. A life cycle assessment of oxymethylene ether synthesis from biomass-derived syngas as a diesel additive. *J Clean Prod* 2017; 165: 1249–1262.

12. Damyanov A, Hofmann P, Pichler TM, et al. Biogenous Ethers - Production and Operation in a Diesel Engine. *MTZ Worldw* 2019; 80: 66–71.

13. Deutz S, Bongartz D, Heuser B, et al. Cleaner production of cleaner fuels: Wind-to-wheel-environmental assessment of CO2-based oxymethylene ether as a drop-in fuel. *Energy Environ Sci* 2018; 11: 331–343.

14. Härtl M, Seidenspinner P, Jacob E, et al. Oxygenate screening on a heavy-duty diesel engine and emission characteristics of highly oxygenated oxymethylene ether fuel OME1. *Fuel* 2015; 153: 328–335.

15. Dworschak P, Berger V, Härtl M, et al. Neat Oxymethylene Ethers: Combustion Performance and Emissions of OME 2 , OME 3 , OME 4 and OME 5 in a Single-Cylinder Diesel Engine. In: *SAE Technical Papers*., 2020: 2020-01-0805.

16. Pastor J V., García-Oliver JM, Micó C, et al. An experimental study with renewable fuels using ECN Spray A and D nozzles. *Int J Engine Res* 2021; 146808742110312.

17. Omari A, Heuser B, Pischinger S, et al. Potential of long-chain oxymethylene ether and oxymethylene ether-diesel blends for ultra-low emission engines. *Appl Energy* 2019; 239: 1242–1249.

18. Gelner AD, Beck HA, Pastoetter C, et al. Ultra-low emissions of a heavy-duty engine

powered with oxymethylene ethers (OME) under stationary and transient driving conditions. *Int J Engine Res* 2022; 23: 738–753.

19. Sharma N, Preuss J, Sjöblom J. Morphological characterization of soot from a compression ignition engine fueled with diesel and an oxygenated fuel. *Int J Engine Res* 2022; 146808742110739.

20. Pellegrini L, Marchionna M, Patrini R, et al. Combustion behaviour and emission performance of neat and blended polyoxymethylene dimethyl ethers in a light-duty diesel engine. *SAE Tech Pap*., 2012: 2012-01-1053.

21. Pélerin D, Gaukel K, Härtl M, et al. Potentials to simplify the engine system using the alternative diesel fuels oxymethylene ether OME1 and OME3−6 on a heavy-duty engine. *Fuel* 2020; 259: 116231.

22. Barro C, Parravicini M, Boulouchos K. Neat polyoxymethylene dimethyl ether in a diesel engine; part 1: Detailed combustion analysis. *Fuel* 2019; 256: 115892.

23. García A, Monsalve-Serrano J, Villalta D, et al. Potential of e-Fischer Tropsch diesel and oxymethyl-ether (OMEx) as fuels for the dual-mode dual-fuel concept. *Appl Energy* 2019; 253: 113622.

24. Barro C, Parravicini M, Boulouchos K, et al. Neat polyoxymethylene dimethyl ether in a diesel engine; part 2: Exhaust emission analysis. *Fuel* 2018; 234: 1414–1421.

25. Pastor JV, García A, Micó C, et al. An optical investigation of Fischer-Tropsch diesel and Oxymethylene dimethyl ether impact on combustion process for CI engines. *Appl Energy*, 2020; 260: 114238.

26. Science C. Converge CFD software, https://convergecfd.com/ (2021, accessed 21 July 2021).

27. Pang KM, Ng HK, Gan S. Light-duty diesel engine modelling with integrated detailed

chemistry in 3-D CFD study. In: *ICEE 2009 - Proceeding 2009 3rd International Conference on Energy and Environment: Advancement Towards Global Sustainability*. 2009, pp. 266–271.

28. Jafari B, Seddiq M. Effects of fuel injection strategies in a RCCI heavy-duty diesel engine. *Sādhanā* 2021; 46: 6.

29. Babayev R, Andersson A, Serra Dalmau A, et al. Computational comparison of the conventional diesel and hydrogen direct-injection compression-ignition combustion engines. *Fuel* 2022; 307: 121909.

30. Pitz WJ, Mueller CJ. Recent progress in the development of diesel surrogate fuels. *Progress in Energy and Combustion Science* 2011; 37: 330–350.

31. Diez A, Crookes RJ, Løvås T. Experimental studies of autoignition and soot formation of diesel surrogate fuels. *Proc Inst Mech Eng Part D J Automob Eng* 2013; 227: 656–664.

32. Lautenschütz L, Oestreich D, Seidenspinner P, et al. Physico-chemical properties and fuel characteristics of oxymethylene dialkyl ethers. *Fuel* 2016; 173: 129–137.

33. O'Rourke PJ, Amsden AA. A particle numerical model for wall film dynamics in port-injected engines. *SAE Tech Pap*., 1996: 961961.

34. Amsden AA, O'Rourke PJ, Butler TD. KIVA-II: A Computer Program for Chemically Reactive Flows with Sprays. *Los Alamos National Lab.,* 1989; LA-11560-MS.

35. Richards KJ, Senecal PK, Pomraning E. CONVERGE 3.0 Manual.

36. Reitz RD, Bracco F V. Mechanisms of breakup of round liquid jets. *Encycl Fluid Mech* 1986; 233–249.

37. Senecal PK, Richards KJ, Pomraning E, et al. A new parallel cut-cell cartesian CFD code for rapid grid generation applied to in-cylinder diesel engine simulations. *SAE Tech Pap*., 2007: 2007-01-0159.

518 38. Naber JD, Reitz RD. Modeling engine spray/wall impingement. *SAE Tech Pap*., 1988:
519 880107.

520 39. Schmidt DP, Rutland CJ. A New Droplet Collision Algorithm. *J Comput Phys* 2000; 164:
521 62–80.

522 40. Desantes JM, Garcia-Oliver JM, Novella R, et al. A numerical study of the effect of
523 nozzle diameter on diesel combustion ignition and flame stabilization. *Int J Engine Res*
524 2020; 21: 101–121.

525 41. Mira D, Pérez-Sánchez EJ, Surapaneni A, et al. LES Study on Spray Combustion With
526 Renewable Fuels Under ECN Spray-A Conditions. In: *ASME 2021 Internal Combustion*
527 *Engine Division Fall Technical Conference*. American Society of Mechanical Engineers.
528 Epub ahead of print 13 October 2021. DOI: 10.1115/ICEF2021-67745.

529 42. Payri F, Olmeda P, Martín J, et al. A complete 0D thermodynamic predictive model for
530 direct injection diesel engines. *Appl Energy* 2011; 88: 4632–4641.

531 43. Pastor J V., Garcia A, Micó C, et al. PIV and DBI Experimental Characterization of Air
532 Flow-Spray Interaction and Soot Formation in a Single Cylinder Optical Diesel Engine
533 Using a Real Bowl Geometry Piston. *SAE Tech Pap*, 2019: 2019-24-0100.

534 44. Senecal PK, Pomraning E, Richards KJ, et al. Multi-dimensional modeling of direct-
535 injection diesel spray liquid length and flame lift-off length using cfd and parallel
536 detailed chemistry. *SAE Tech Pap*., 2003: 2003-01-1043.

537 45. Cai L, Jacobs S, Langer R, et al. Auto-ignition of oxymethylene ethers (OMEn, n = 2–4) as
538 promising synthetic e-fuels from renewable electricity: shock tube experiments and
539 automatic mechanism generation. *Fuel* 2020; 264: 116711.

540 46. Nordin N. *Numerical Simulations of Non-Steady Spray Combustion Using a Detailed*
541 *Chemistry Approach*. Chalmers University of Technology, 1998.

47. Hiroyasu H, Kadota T. Models for Combustion and Formation of Nitric Oxide and Soot in Direct Injection Diesel Engines. *SAE Prepr*., 1976: 760129.

48. Pastor J V., García A, Micó C, et al. Simultaneous high-speed spectroscopy and 2-color pyrometry analysis in an optical compression ignition engine fueled with OMEX-diesel blends. *Combust Flame* 2021; 230: 111437.

49. Dec JE, Coy EB. OH radical imaging in a di diesel engine and the structure of the early diffusion flame. *SAE Tech Pap*., 1996: 960831.

50. Pastor J V., García-Oliver JM, Micó C, et al. Experimental Study of the Effect of Hydrotreated Vegetable Oil and Oxymethylene Ethers on Main Spray and Combustion Characteristics under Engine Combustion Network Spray A Conditions. *Appl Sci* 2020; 10: 5460.

51. Ibrahim F, Wan Mahmood WMF, Abdullah S, et al. Comparison of Simple and Detailed Soot Models in the Study of Soot Formation in a Compression Ignition Diesel Engine. *SAE Tech Pap*., 2017: 2017-01-1006.

52. Payri F, García-Oliver JM, Novella R, et al. Influence of the n-dodecane chemical mechanism on the CFD modelling of the diesel-like ECN Spray A flame structure at different ambient conditions. *Combust Flame* 2019; 208: 198–218.

53. Goeb D, Davidovic M, Cai L, et al. Oxymethylene ether – n-dodecane blend spray combustion: Experimental study and large-eddy simulations. *Proc Combust Inst* 2021; 38: 3417–3425.

54. Pickett LM, Kook S, Williams TC. Visualization of Diesel Spray Penetration, Cool-Flame, Ignition, High-Temperature Combustion, and Soot Formation Using High-Speed Imaging. *SAE Int J Engines* 2009; 2: 2009-01–0658.

55. Honecker C, Neumann M, Glueck S, et al. Optical Spray Investigations on OME3-5 in a Constant Volume High Pressure Chamber. In: *SAE Technical Papers*., 2019: 2019-24-

0234.

6. APPENDIX

SPRAY CONE ANGLE CALCULATION

To calculate the spray cone angle to configure the spray model, the natural luminosity images used by Pastor et al.[25] where utilized. The thermal radiation from early combustion during the main injection event allowed to identify and characterize the sprays geometry between 3° and 6° aTDC. For this images, a segmentation algorithm extensively used by the Engine Combustion Network[54] was applied to each of the sprays to obtain the spray contour and, from it, calculate the spray cone angle. In Figure 13, an example of one of the images used for this purpose is shown, together with the contours detected in green. As it can be observed, the morphology detected can be influenced by the flame appearing at the edge of the bowl. To avoid this, the three most affected sprays (highlighted by a yellow box) were not considered in the analysis. Besides, only a sector between the 10 and 60% of the spray total length was considered for the calculations. The two red circles represented in Figure 13 help identifying this region.

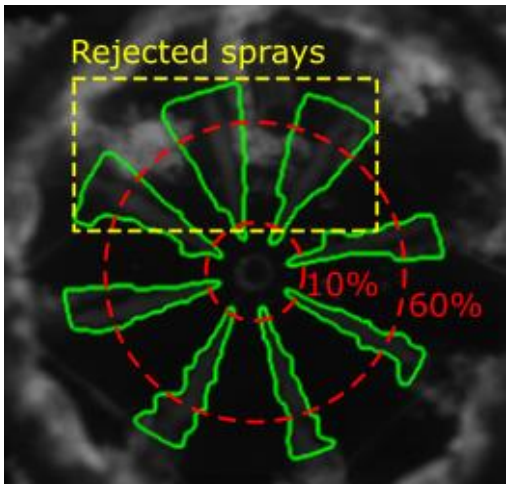

Figure 13 Example of a Diesel combustion natural luminosity image used to calculate spray cone angle. The green lines represent the contours detected by the processing algorithm and used to calculate the spray angle and the red circles represent the sector of the sprays considered for angle calculation.

The procedure described in the previous paragraph was applied for Diesel images, corresponding to the start of the main injection combustion event (between 3 and 5.7° aTDC). Based on 5 out of the 8 sprays, for 9 consecutive images and 3 consecutive combustion cycles, an average value of 15.25° was obtained with a standard deviation of 1.75°. For OME_X, it was not possible to follow this approach due to the absence of soot and thermal radiation. According to the data presented by Honecker et al.[55], small differences could be expected between both fuels. However, it has a strong dependency on in-cylinder temperature as opposite trends between both fuels were observed when increasing temperature from 800 to 850 K in a high-pressure vessel. Considering this, in addition to the standard deviation obtained for Diesel, it has been decided to use 15.25° for OME_X too.